

Fabrication and characterization of free-standing, high-line-density transmission gratings for the vacuum UV to soft X-ray range

S.J. Goh,^{1*} H.J.M. Bastiaens,¹ B Vratzov,^{1,2} Q. Huang,³ F. Bijkerk,^{1,3} and K.J. Boller¹

¹Laser Physics and Nonlinear Optics, Mesa + Institute for Nanotechnology, University of Twente, Enschede, The Netherlands

²NT&D—Nanotechnology and Devices, Wirichsbongardstraße 24, 52062 Aachen, Germany

³Industrial Focus Group XUV Optics, MESA + Institute for Nanotechnology, University of Twente, PO Box 217, 7500 AE Enschede, The Netherlands

*s.j.goh@utwente.nl

Abstract: We present state-of-the-art high resolution transmission gratings, applicable for spectroscopy in the vacuum ultraviolet (VUV) and the soft X-ray (SRX) wavelength range, fabricated with a novel process using ultraviolet based nano imprint lithography (UV-NIL). Free-standing, high-line-density gratings with up to 10,000 lines per mm and various space-to-period ratios were fabricated. An optical characterization of the gratings was carried out in the range from 17 to 34 nm wavelength using high-harmonic generation in a capillary waveguide filled with Ne, and around 13.5 nm wavelength (from 10 to 17 nm) using a Xenon discharge plasma.

©2015 Optical Society of America

OCIS codes: (050.1950) Diffraction gratings; (220.3740) Lithography; (340.7480) X-rays, soft x-rays, extreme ultraviolet (EUV).

References and links

1. J. A. Carlisle, E. L. Shirley, E. A. Hudson, L. J. Terminello, T. A. Callcott, J. J. Jia, D. L. Ederer, R. C. C. Perera, and F. J. Himpsel, "Probing the Graphite band structure with resonant soft-X-Ray fluorescence," *Phys. Rev. Lett.* **74**(7), 1234–1237 (1995).
2. C. Wagner and N. Harned, "EUV LITHOGRAPHY Lithography gets extreme," *Nat. Photonics* **4**(1), 24–26 (2010).
3. V. Bakshi, *EUV Sources for Lithography* (Society of Photo Optical, 2006).
4. J. Ullrich, A. Rudenko, and R. Moshhammer, "Free-Electron Lasers: New avenues in molecular physics and photochemistry," *Annu. Rev. Phys. Chem.* **63**(1), 635–660 (2012).
5. K. Wilhelm, B. N. Dwivedi, E. Marsch, and U. Feldman, "Observations of the sun at vacuum-ultraviolet wavelengths from space. Part I: Concepts and instrumentation," *Space Sci. Rev.* **111**(3/4), 415–480 (2004).
6. R. de Bruijn, K. Koshelev, G. Kooijman, E. S. Toma, and F. Bijkerk, "Absorption of EUV in laser plasmas generated on xenon gas jets," *J. Quant. Spectrosc. Ra.* **81**(1–4), 97–105 (2003).
7. M. J. Word, I. Adesida, and P. R. Berger, "Nanometer-period gratings in hydrogen silsesquioxane fabricated by electron beam lithography," *J. Vac. Sci. Technol. B* **21**(6), L12–L15 (2003).
8. T. A. Savas, M. L. Schattenburg, J. M. Carter, and H. I. Smith, "Large-area achromatic interferometric lithography for 100 nm period gratings and grids," *J. Vac. Sci. Technol. B* **14**(6), 4167–4170 (1996).
9. D. R. McMullin, D. L. Judge, C. Tarrío, R. E. Vest, and F. Hanser, "Extreme-ultraviolet efficiency measurements of freestanding transmission gratings," *Appl. Opt.* **43**(19), 3797–3801 (2004).
10. B. Vratzov, A. Fuchs, M. Lemme, W. Henschel, and H. Kurz, "Large scale ultraviolet-based nanoimprint lithography," *J. Vac. Sci. Technol. B* **21**(6), 2760–2764 (2003).
11. H. W. Schnopper, L. P. Van Speybroeck, J. P. Delvaille, A. Epstein, E. Källne, R. Z. Bachrach, J. Dijkstra, and L. Lantward, "Diffraction Grating Transmission Efficiencies for Xuv and Soft X Rays," *Appl. Opt.* **16**(4), 1088–1091 (1977).
12. M. Born and E. Wolf, *Principles of Optics: Electromagnetic Theory of Propagation, Interference and Diffraction of Light* 6th ed. (Pergamon, 1980), xxvii, 808 p.
13. The Center for X-Ray Optics website: [www.cxro.lbl.gov].
14. S. Sailaja, V. Arora, S. R. Kumbhare, P. A. Naik, P. D. Gupta, D. A. Fedin, A. A. Rupasov, and A. S. Shikanov, "A simple XUV transmission grating spectrograph with sub-angstrom resolution for laser-plasma interaction studies," *Meas. Sci. Technol.* **9**(9), 1462–1468 (1998).
15. C. Palmer, *Diffraction Grating Handbook* 6th ed. (Newport Corporation), Chap. 8.

16. C. G. Wahlström, J. Larsson, A. Persson, T. Starczewski, S. Svanberg, P. Salières, P. Balcou, and A. L'Huillier, "High-Order Harmonic Generation in Rare Gases with an Intense Short-Pulse Laser," *Phys. Rev. A* **48**(6), 4709–4720 (1993).
17. P. Balcou, P. Salieres, K. S. Budil, T. Ditmire, M. D. Perry, and A. Lhuillier, "High-Order Harmonic-Generation in Rare-Gases - a New Source in Photoionization Spectroscopy," *Z. Phys. D Atom. Mol. Cl.* **34**(2), 107–110 (1995).
18. P. B. Corkum, "Plasma Perspective on Strong Field Multiphoton Ionization," *Phys. Rev. Lett.* **71**(13), 1994–1997 (1993).
19. RSoft DiffractMOD, "RSoft Design Group." <http://www.rsoftdesign.com>.
20. N. M. Ceglio, A. M. Hawryluk, D. G. Stearns, M. Kühne, and P. Müller, "Demonstration of Guided-Wave Phenomena at Extreme-Ultraviolet and Soft-X-Ray Wavelengths," *Opt. Lett.* **13**(4), 267–269 (1988).
21. T. H. Markert, D. Dewey, J. E. Davis, K. A. Flanagan, D. E. Graessle, J. M. Bauer, and C. S. Nelson, "Modeling the diffraction efficiencies of the AXAF high energy transmission gratings," *Euv, X-Ray, and Gamma-Ray Instrumentation for Astronomy VI* **2518**, 424–437 (1995).
22. G. Reichardt and F. Schafers, "Laminar versus trapezoidal grating profiles: AFM-measurements and efficiency simulations," *Gratings and Grating Monochromators for Synchrotron Radiation* **3150**, 121–129 (1997).
23. P. Desaute, H. Merdji, V. Greiner, T. Missalla, C. Chenais-Popovics, and P. Troussel, "Characterization of a high resolution transmission grating," *Opt. Commun.* **173**(1–6), 37–43 (2000).
24. A. Bouhal, R. Evans, G. Grillon, A. Mysyrowicz, P. Breger, P. Agostini, R. C. Constantinescu, H. G. Muller, and D. von der Linde, "Cross-correlation measurement of femtosecond noncollinear high-order harmonics," *J. Opt. Soc. Am. B* **14**(4), 950–956 (1997).
25. C. G. Durfee, A. R. Rundquist, S. Backus, C. Herne, M. M. Murnane, and H. C. Kapteyn, "Phase matching of high-order harmonics in hollow waveguides," *Phys. Rev. Lett.* **83**(11), 2187–2190 (1999).
26. N. B. D. M. V. Ammosov and V. P. Krainov, "Tunnel ionization of complex atoms and of atomic ions in an alternating electromagnetic field," *Sov. Phys. JETP-USSR* **64**(6), 1191 (1986).
27. E. R. Kieft, J. J. A. M. van der Mullen, G. M. W. Kroesen, and V. Banine, "Time-resolved pinhole camera imaging and extreme ultraviolet spectrometry on a hollow cathode discharge in xenon," *Phys. Rev. E Stat. Nonlin. Soft Matter Phys.* **68**(5), 056403 (2003).

1. Introduction

The wavelength band from the vacuum ultra-violet (VUV, 200 to 10 nm) to the soft-x-ray range (SXR, 20 to 2 nm), also referred to the XUV band, is highly relevant for a number of important applications and research fields. These include fluorescence analysis of materials in the SXR band [1], high resolution photolithography in the XUV [2, 3], research at free electron lasers in the SXR band [4], and XUV space research [5]. The spectral analysis of radiation in these wavelength ranges requires dispersive elements with adequate spectral resolution.

XUV spectrometers based on *transmission* gratings [6] are of significant relevance because they offer a number of important advantages, such as compactness and ease in alignment at normal incidence, compared to reflective gratings which use grazing incidence. Due to the free-standing geometry, light is transmitted directly through the open space between the lines of the grating. Therefore, the transmitted power spectral density is approximately independent of the wavelength, which eases calibration. Combining transmission gratings with, e.g. back illuminated CCD cameras, compact and easy-to-operate XUV spectrometers can be built.

To accommodate for a specific application, the line density of a transmission grating needs to be tailored to provide sufficient spectral resolution in the wavelength range of interest. For instance, to characterize an XUV light source emitting at around 13.5 nm or 6.8 nm, it turns out that extremely dense gratings near current nanofabrication limits are required due to the short wavelength. Specifically, grating periods in the order of 100 nm (i.e. 10,000 lines per mm) are required to achieve a resolution of at least a few tenths of nm. To maximize the free spectral range, undesired diffraction orders need to be suppressed by choosing an appropriate space-to-period ratio. This imposes strict demands regarding the fabrication accuracy of the space-to-period ratio. Furthermore, it needs to be considered that fabrication of narrow lines implies that the thickness of the lines is small as well. This can lead to an undesired residual transmission of light through the lines, which reduces the contrast of the grating transmission function. As a result, the fabrication of free-standing transmission

gratings with high line density, accurate space-to-period ratio and appropriate line thickness is extremely challenging even with state-of-the-art nanolithography. The current fabrication methods for high-density transmission gratings include electron beam lithography (EBL) [7] and interferometric lithography (IL) [8, 9]. However, EBL provides a relatively low throughput, while IL has a limited resolution.

In this paper, we apply UV based nano imprint lithography (UV-NIL) using a lift-off and back etch process to fabricate the gratings. This fabrication method has been shown to obtain high resolution and highly reproducible nanometer-scale structures [10]. Furthermore, the resolution is comparable to the high resolution of electron beam lithography, however, with much higher throughput in fabrication. Essential for the development of the overall grating fabrication process and the associated costs is the relatively fast and straightforward parallel printing nature of NIL. The latter allows fabrication of many slightly different gratings in a single step, which facilitates the optimization for the various lift-off and back etch processes with the goal to improve the quality of the fabrication process. Once optimized, this feature also allows the fabrication of a set of gratings with different line densities in a single batch.

This paper describes the first fabrication and optical characterization of free-standing, high-line-density gratings based on UV-NIL. The optical characterization is important for quantifying the relative strength of higher diffraction orders, particularly the second order, which depends on imperfections in fabrication that might lead, e.g. an asymmetric space-to-period ratio. Such imperfections in grating features cannot be observed via a morphological analysis alone, such as based on Scanning Electron Microscopy (SEM). An optical characterization is also important for evaluating the spectral resolution that can be achieved. The characterization requires XUV sources with appropriate spatial and spectral coherence. Here we use an XUV sources. The first is based on high harmonic generation (HHG), which offers a high spatial coherence and a well-structured spectrum comprising a distinct and known set of wavelengths across the entire range from 17.5 nm to 40.5 nm. The second source is based on a Xenon plasma emitting in the range around 13.5 nm.

In the following Sect. 2, we describe the experimental setup in which the gratings were characterized, and we present the design criteria and the fabrication method for the transmission gratings. In Sect. 3, we discuss the results obtained with the optical characterization. Special emphasis is put on the comparison of gratings that differ in their space-to-period ratio but possess the same grating period, and on measuring the experimental resolution for a comparison with the theoretically expected values.

2. Experimental details

2.1 Transmission grating spectrometer

Figure 1(a) gives an overview of the transmission grating spectrometer setup, which comprises an incident beam (here from a high harmonic source or a plasma source), an entrance slit and a transmission grating. The diffracted light falls on a detector, which is the chip of a back-illuminated CCD camera (Andor, DO420-BN). The advantages of such setup are that the spectral range and spectral resolution can be adjusted easily via the distance from the grating to the detector, that a relatively high first-order diffraction efficiency is achieved, and that the diffraction efficiency is nearly independent of the wavelength. Figure 1(b) illustrates the front view and cross section of one of the transmission gratings. It can be seen that the overall grating dimension is 4 mm × 1 mm, divided up into 2666 separate areas (five areas are shown schematically), each being 1200 nm high, separated by 300 nm wide support bars. The support bars are required for the mechanical stability of the grating in view of its large area. The actual line structure of the grating shown in Fig. 1(c) consists of equidistant parallel grating lines of $b = 50$ nm width, spaced by $a = 50$ nm, to yield a grating period of $d = 100$ nm. The cross section of the grating lines consists of a 200 nm thick Si₃N₄ layer, a 70 nm thick Au layer and a 12 nm thick Cr layer, carried on a 380 μm thick Si wafer.

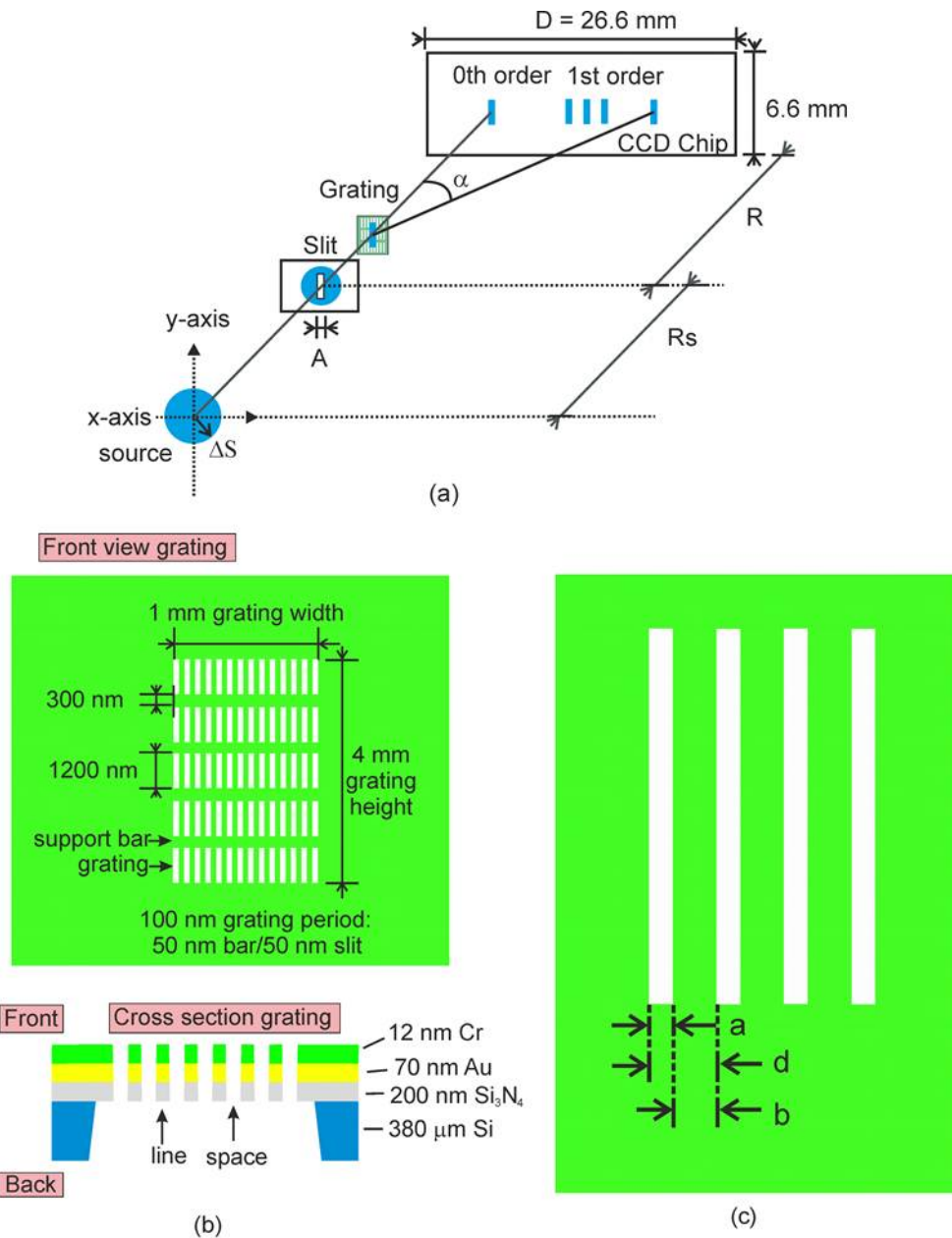


Fig. 1. (a) Transmission grating spectrometer setup, (b) enlarged view of a transmission grating with a density of $10,000 \text{ lines mm}^{-1}$, (c) definition of the grating parameters d (period), a (space) and b (line width)

In the following, to prepare for comparison with experimental data, we briefly recall some basic relations describing diffraction at a grating. We assume that the grating-detector distance, R , is much larger than the space between two grating lines, a , which is fulfilled here. For a plane wave that is normally incident on the grating, the diffraction angle for a wavelength λ is given by the well-known grating equation

$$d \sin \alpha = m\lambda, \quad (1)$$

where d is the grating period, α is the diffraction angle and m is the diffraction order. As can be seen from Eq. (1), when an incident beam with a wide range of wavelengths is incident on the grating, the spectra belonging to neighboring orders may partially overlap. The spectral width across which overlapping does not occur is known as the free spectral range. To maximize the free spectral range, the power diffracted into orders bigger than one is desired to be minimal. A limitation of the spectral range that can be observed towards long wavelengths, thereby limiting the free spectral range as well, is given by the detector size and geometry as

$$\lambda_{\max} = \frac{d}{m} \sin[\tan^{-1}(\frac{D}{R})], \quad (2)$$

where D is the transverse dimension of the CCD chip and where R is the grating-detector distance. To cover the part of the XUV band that is of interest here, i.e. the wavelength range to be covered by our HHG source (from 17.5 nm to 40.5 nm) and the range to be covered by the Xe plasma source (10 nm to 17 nm), a free spectral range from 10 nm to 40.5 nm is required. For our setup, where $D = 26.6$ mm and $d = 100$ nm (with $m = 1$) we have chosen $R = 60$ mm, which yields $\lambda_{\max} = 40.5$ nm. Importantly, with this combination of incident wavelengths, grating period and geometry (D/R), it should become possible to observe the first-order and second-order diffraction simultaneously for wavelengths between 17.5 nm and 20.25 nm. Thereby the second-order diffraction efficiency and the degree of suppression of second-order diffraction vs. grating geometry (i.e. space-to-period ratio) can be easily quantified, as will be described in detail below.

To calculate the efficiency for the various diffraction orders, we begin with considering opaque grating lines and use a model [11] based on Kirchhoff's diffraction theory in the Fraunhofer approximation [12]. We note that considering the lines as fully opaque, as if made from a perfect metal, is done here only as an approximation. To account for the finite transmission of real metals in the XUV, we later replace the approximation and also model the grating with partially transparent lines [Eq. (5)]. The Fraunhofer approximation can be expressed as the conditions $\frac{a^2}{R\lambda} \ll 1$ and $\frac{a^2}{R_s\lambda} \ll 1$, which are fulfilled here because the

grating slit width, a , is larger than or comparable with the wavelength, λ , but is very small compared to the distances R_s and R [see Fig. 1]. The model is further simplified by using a one-dimensional analysis with the assumption that the grating consists of very long equidistant parallel slits. We hereby neglect the secondary interference pattern introduced by the grating support bars that extends vertically in Fig. 1(a). With these approximations, the diffraction efficiency, η_m , of the m^{th} order is given by [11]

$$\eta_m = \left[\frac{\sin(m\pi \frac{a}{d})}{m\pi} \right]^2. \quad (3)$$

The ratio of power in the m^{th} order with regard to the first order is then obtained as

$$T_{m/1} = \frac{\eta_m}{\eta_1} = \left(\frac{\sin\left(m\pi \frac{a}{d}\right)}{m \sin\left(\pi \frac{a}{d}\right)} \right)^2. \quad (4)$$

From Eq. (4) it can be seen that choosing a symmetric grating characterized by a space-to-period ratio, $\mu = a/d = 0.5$, we obtain $T_{2/1} = 0$. This corresponds to the ideal case that the 2nd

order is fully suppressed, thereby effectively doubling the free spectral range. What can be seen from Eq. (4) as well, valid when the grating lines are completely opaque, is that the calibration of the optical power spectral density of the grating is straightforward because the diffraction efficiency of the first and all higher orders would be independent of the wavelength. However, the lines of the grating investigated here might not be completely opaque due to their small thickness which is the result of a limited aspect ratio in etching narrow lines. In the wavelength range considered here the absorption lengths for the materials used (Si_3N_4 , Au, and Cr) lie in the range between 1 and 10 nm. The residual transmission of light which propagates through the grating lines, and the wavelength dependent phase shift of that light, will lead to a diffraction efficiency that is not spectrally flat, which would have to be taken into account in an accurate spectral calibration of the grating. In order to predict in how far such effects would play a role for the gratings with our dimensions and to justify additional fabrication steps that could avoid these effects, we look at the first-order diffraction efficiency versus wavelength for a grating with partially transmitting lines [11]

$$\eta_m(\lambda) = \left(\frac{\sin(m\pi\mu)}{m\pi} \right)^2 \left[1 + \exp\left(-\frac{4\pi n_2 z_0}{\lambda}\right) - 2 \exp\left(-\frac{2\pi n_2 z_0}{\lambda}\right) \cos\left(\frac{2\pi(n_1 - 1)z_0}{\lambda}\right) \right]. \quad (5)$$

Here $n = n_1 + in_2$ is the complex, wavelength-dependent refractive index of the grating line material, z_0 is the thickness of the grating lines and the μ is the space-to-period ratio defined above. The red curve in Fig. 2 shows the first-order diffraction efficiency, calculated with Eq. (5) for a symmetric ($\mu = 0.5$) Si_3N_4 grating with $z_0 = 200$ nm thick lines, which we consider a safe but lower limit of thickness in terms of fabrication. The complex index of Si_3N_4 is taken from [13]. It can be seen that the diffraction efficiency lies around an average value of 10% and that there is indeed quite some spectral variation, particularly in the wavelength range between 13 and 30 nm. To predict whether this undesired effect can be minimized with an additional absorbing layer, we also calculated the spectral response of the Si_3N_4 grating for the case that a more strongly XUV absorbing Au/Cr bilayer of 70/12 nm is deposited on top. The calculation is based on Eq. (5) again, where the sequential transmission through the materials (Si_3N_4 , Au, Cr) was modeled via adding their respective absorbance in the exponentials and via adding their respective phase shifts in the cosine argument. The complex index data were taken from [13]. The first-order efficiency of this grating with increased line opacity is shown in Fig. 2 as the black curve. It can be seen that a much more uniform spectral response is obtained with only a 2% variation around the 10% average.

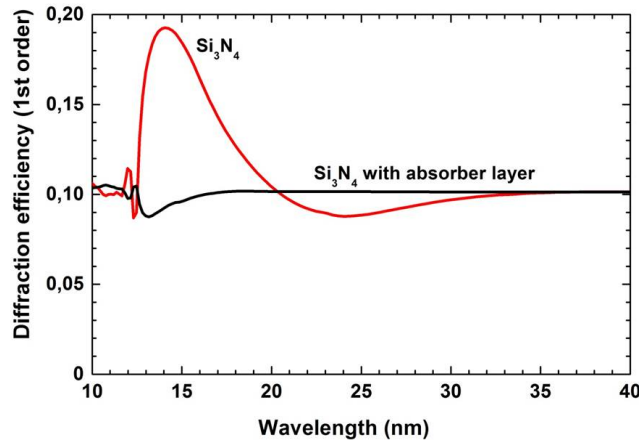


Fig. 2. Calculated spectral variation of the first order diffraction efficiency for a symmetric ($\mu = 0.5$) grating with 200-nm thick Si_3N_4 lines (red curve) and the same grating with an extra 70 nm Au layer and an extra 12 nm Cr layer deposited on the lines (black curve).

As another important characteristic we consider the spectral resolution [14],

$$\Delta\lambda_{th} = \left\{ \left[\frac{d}{m} \left(\frac{\Delta S + A}{R_s} \right) + \frac{d}{m} \left(\frac{K}{R} \right) \right]^2 + \left(\frac{\lambda d}{mA} \right)^2 \right\}^{1/2}, \quad (6)$$

which is determined to a first part by the geometrical resolution (first square term) and to a second part by the dispersive resolution of the grating (second square term). The geometrical resolution takes into account the finite diameter of the source, ΔS , the width of the aperture, A , the width of a CCD-pixel, p , the distance between the source and the grating, R_s , and the distance between the grating and the detector, R . We note that K corresponds to the full width at half-maximum for the convolution of A across p [15]. Equation (6) shows that the achievable spectral resolution depends not only on the parameters of the spectrometer setup, but also on the source, via ΔS and R_s , which will be discussed later in Sect. 3.

2.2. Fabrication of gratings

In the previous section, we have given an example of the desired parameters for the 10,000 lines mm^{-1} gratings which are based on fabrication with a 200 nm thick grating lines made from Si_3N_4 with an Au/Cr bilayer of 70/12 nm on top and a space-to-period ratio of $\mu = 0.5$. Here we describe the fabrication of such gratings using the following lithographic technique. Firstly, a layer of 200 nm Si_3N_4 is deposited on a 400 μm thick Si wafer. The wafer material is to be removed later except for a frame and the 300 nm wide bars to support a free-standing membrane. Si_3N_4 is chosen because this material allows the fabrication of high quality membranes with low and well-controlled internal stress. For defining the grating patterns, we apply UV based nano imprint lithography (UV-NIL) using a single imprint template comprising 21 individual gratings placed over a total area of 16 x 16 mm^2 . The different gratings possess line densities of 500, 780, 1000, 1500 and 1850 mm^{-1} , and from 2000 to 10,000 mm^{-1} in steps of 1000 mm^{-1} . Each grating has a free-standing area of 4 mm height and 1 mm width. The imprints were carried out on an Imprio 55 device (Molecular Imprints, Inc.).

The fabrication process is shown in Fig. 3. First, the substrate is spin-coated at 3000 rpm with a 100 nm thick water solvable transfer layer (UL-300 from Micro Resist Technology GmbH) and then baked at 150 C for 120 s on a proximity hot plate. In the imprint machine, the imprint resist is dispensed on top of the transfer layer [Fig. 3(a)]. The template is then pressed into the imprint resist with a force of 3 N at room temperature. After spreading, the imprint resist is cured with a 3 s UV exposure through the transparent template while the template is still in contact. After that, the template is detached leaving its negative shape in the hardened imprint resist. The patterned layer shows a feature height of 100 nm and a residual layer of 35 nm [Fig. 3(b)]. In the next step, a planarization layer of 160 nm hydrogen silsesquioxane (HSQ), XR-1541 6 (from Dow Corning), is deposited by spin coating on top of the imprinted feature [Fig. 3(c)]. After getting a planarized surface the etch-back of the top layer of HSQ, followed by a pattern transfer through the residual imprint resist and transfer layer [Fig. 3(d)], is carried out using a two-step Reactive Ion Etching (RIE) process in fluorine and oxygen-based plasma. The planarization and etch back RIE process offers very high critical dimension (CD) control as well as a small sidewall undercut as needed for a lift-off process. An XUV absorber layer of Au (70 nm) followed by an etch mask layer of Cr (12 nm) is deposited by metal evaporation using an electron beam deposition tool [Fig. 3(e)]. Then, lift-off to form the top absorber layer and the etch mask for patterning the Si_3N_4 layer is carried out by dipping the sample into deionized water in an ultrasonic bath [Fig. 3(f)]. The openings for the single gratings of 1 mm x 4 mm on the back side are defined by optical lithography followed by a fluorine-based RIE of the Si_3N_4 layer on the backside and a 4 hours wet etch process in potassium hydroxide (KOH) removing the bulk silicon and stopping on the top Si_3N_4 layer [Fig. 3(g)]. The final step in the fabrication of the grating is to etch through

the Si_3N_4 membrane using the Cr layer as a etch mask in the same fluorine-based RIE [Fig. 3(h)].

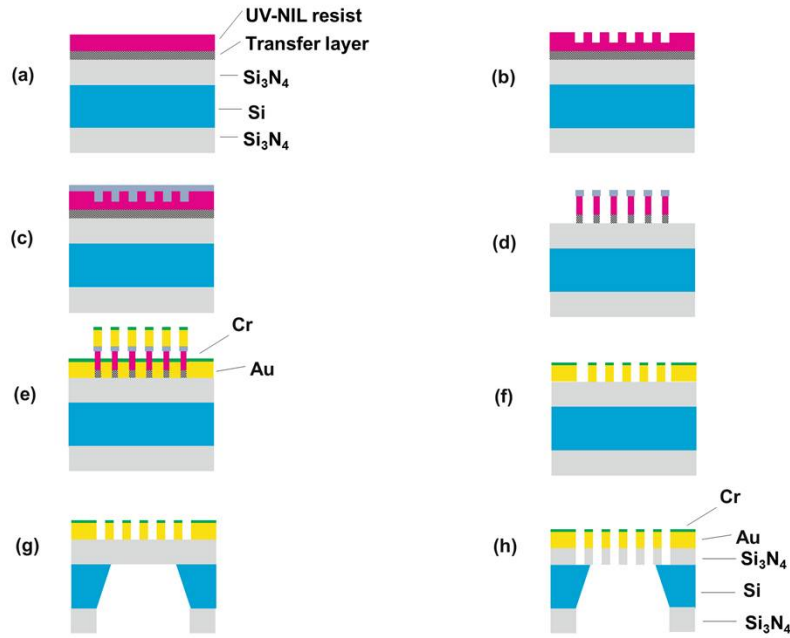


Fig. 3. Process flow for fabrication of the free-standing gratings: (a) deposition of Si_3N_4 and imprint resists on a Si wafer, (b) UV-Nano Imprint Lithography (UV-NIL) for high resolution pattern definition, (c) planarization and etch back of the top layer by Reactive Ion Etching (RIE), (d) pattern transfer down to the Si_3N_4 by RIE with excellent CD control and a small undercut for a lift-off process, (e) deposition of an Au absorber layer and Cr etch mask by evaporation, (f) lift-off to form the top absorber layer and etch mask, (g) back side optical lithography and subsequent patterning of Si_3N_4 by RIE and Si by wet etching, (h) grating definition by RIE etch into Si_3N_4 .

For the highest line density of $10,000 \text{ lines mm}^{-1}$, we have fabricated five different gratings to which we refer as G1, G2, G3, G4 and G5 with a grating space-to-period ratio of $\mu = 0.45, 0.50, 0.50, 0.50$ and 0.55 , respectively. The motivation for fabrication of multiple gratings with the same μ -values (G2, G3, G4) is to obtain a measure for fabrication reproducibility. Different μ -values (G1, G2/G3/G4, G5) have been fabricated as well, in order to increase the chances for realizing an optimized grating with a maximally suppressed second diffraction order. In spite of intrinsic fabrication errors, this approach is relatively cost effective with our NIL fabrication method because all of the five gratings are available on a single imprint template and can be fabricated all at once in a single process.

In order to find out how close to specifications our gratings are, we started characterizing the gratings with recording SEM images. Figure 4 shows, as an example, a SEM image of grating G3 (design goal $\mu = 0.5$). It can be seen that the grating is highly periodic as desired, and that the width of the grating lines is rather uniform. The SEM images of the other gratings (G1, G2, G4, G5) exhibit similarly high periodicity and uniformity.

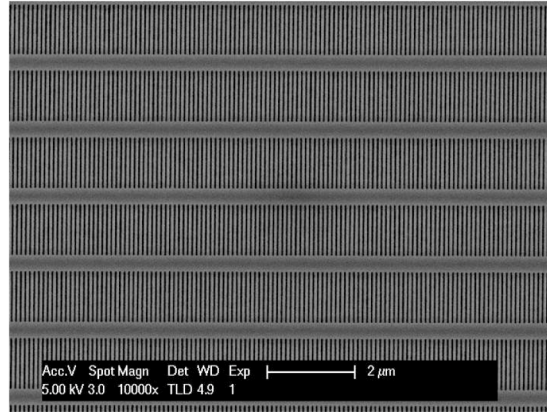


Fig. 4. Scanning electron microscopy image for the 10,000 lines mm^{-1} grating G3 (design for $\mu = 50/50$).

A quantitative evaluation of the fabricated average space-to-period ratio, $\bar{\mu}$, of the gratings is carried out by measuring 30 different sampling points (space-to-period ratios) from each of their corresponding SEM image. The evaluation reveals that, for all the gratings, $\bar{\mu}$ is close to the intended design ratio, μ , with a standard deviation around $\sigma = 0.04$, as shown in Fig. 5. To obtain a measure for fabrication reproducibility of different gratings with the same design goal, we calculated the standard deviation from the measured $\bar{\mu}$ -values of the gratings G3, G4 and G5 ($\mu = 0.5$). This yields a value of 0.02, corresponding to a reproducibility of 4 nm for the width of the grating lines.

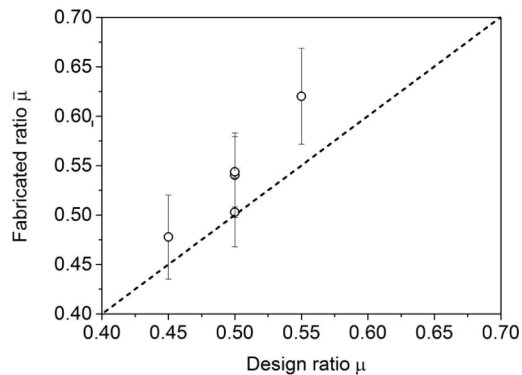


Fig. 5. Fabricated average space-to-period ratios, $\bar{\mu}$, determined from the SEM images for the gratings G1, G2/G3/G4 and G5 versus the intended design ratios, μ , of 0.45, 0.5 and 0.55. The full length of the error bars is taken as 2σ , where σ is the standard deviation measured in the SEM images for each grating. The dashed line indicates the ideal case of zero fabrication error.

3. XUV optical characterization and discussion

For an optical characterization we used two different XUV sources. The first is based on high harmonic generation (HHG) which is available in table-top scale and easily accessible as compared to, e.g. a synchrotron source. The HHG output possesses an excellent spatial coherence resulting in a low divergence beam (~ 0.1 mrad), and it offers a well-structured spectrum comprising a distinct set of known wavelengths. The radiation is generated via a highly nonlinear optical process that produces ultrashort pulses with a broad spectrum including XUV radiation, obtained by focusing ultrahigh intensity infrared laser pulses into a

gaseous medium, typically a noble gas [16, 17]. The experimental setup for the XUV source is schematically shown in Fig. 6. To drive the HHG, we employ a pulsed Ti:Sapphire infrared (IR) laser with 780 nm center wavelength at 1 kHz repetition rate (Legend Elite Duo HP USP, Coherent Inc.). The duration of the IR laser pulses is 39 fs with a pulse energy of 6.5 mJ. A 67 mm long capillary-waveguide with a 508 μm wide inner diameter is mounted in a vacuum chamber and is filled with Ne gas at 40 mbar. For mode matching the drive laser beam to the lowest order waveguiding capillary mode, we use a focusing mirror with a focal length of 2.5 m. Taking into account the coupling efficiency of the IR laser radiation into the capillary, the peak intensity launched into the waveguide is $2.6 \times 10^{14} \text{ W/cm}^2$. The cut-off wavelength of HHG, which is the shortest wavelength that can be generated [18], decreases with increasing drive laser intensity and ionization potential of the used type of noble gas. In order to observe the first-order and second-order diffraction simultaneously for wavelengths between 10 nm and 20.25 nm, we chose to use the noble gas Ne due to its relatively high ionization potential, 21.6 eV. With the cut-off law [18], we determine theoretically that the obtainable cut-off wavelength from the high harmonic source is 17.5 nm (45th harmonic order), which is suitable for the experiments. Behind the capillary, we let the high harmonic and drive laser beams co-propagate over a distance of 9 m, for reducing the drive laser intensity by diffraction. The drive laser beam is then blocked by a set of two Aluminium (Al) filters placed in series, each of them 200 nm thick. The XUV radiation is sent to the transmission grating spectrometer [see Fig. 1(a)] for spectral measurements. The Al filters also act as a bandpass for XUV radiation, limiting the spectral transmission of the path to the CCD detector to a range from 16 nm to 40 nm. This range is, however, sufficient to detect all the relevant output wavelengths of the harmonic source.

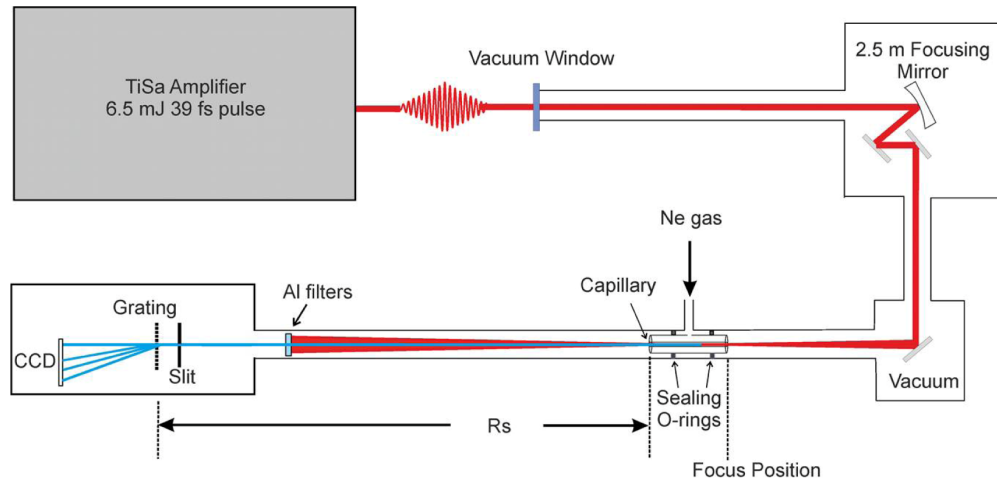


Fig. 6. Table-top XUV source based on high harmonic generation (HHG) with a Ne-filled capillary.

For a first step of optical characterization of the gratings, we have recorded series of spectra of the HH beam, using the five different gratings G1 to G5. Figure 7(a) shows an example of such spectral measurement, in this case performed with G3. The measurement shows that the grating is resolving the various high order harmonics; that only odd harmonics are generated is a typical characteristic of such a source. The highest harmonic order that we observe in the spectrum is the 45th harmonic order at a wavelength 17.5 nm, which matches very well with the theoretical value for the cutoff wavelength.

With the geometry of our setup, the second diffraction order for harmonic orders lower than the 39th is not measurable as they fall out of the detector image range (λ_{max} limited by D in Eq. (2)). However, although the intensity of the second-order diffraction peak is small [as

was actually intended via choosing $\mu = 0.5$), there are several harmonic orders (from 39th to 45th) of which we can record the first and second diffraction order simultaneously. This simultaneous appearance, resulting from our choice of suitable parameters (Ne-gas, peak intensity of $2.6 \times 10^{14} \text{ W/cm}^2$, grating period, $d = 100 \text{ nm}$, $D = 26.6 \text{ mm}$ and $R = 600 \text{ mm}$), is what enables to extract the ratio of 2nd to 1st order ratio of diffraction efficiency, $\eta_2/\eta_1 = T_{2/1}$, and compare it with the theoretically expected value that should depend on $\bar{\mu}$.

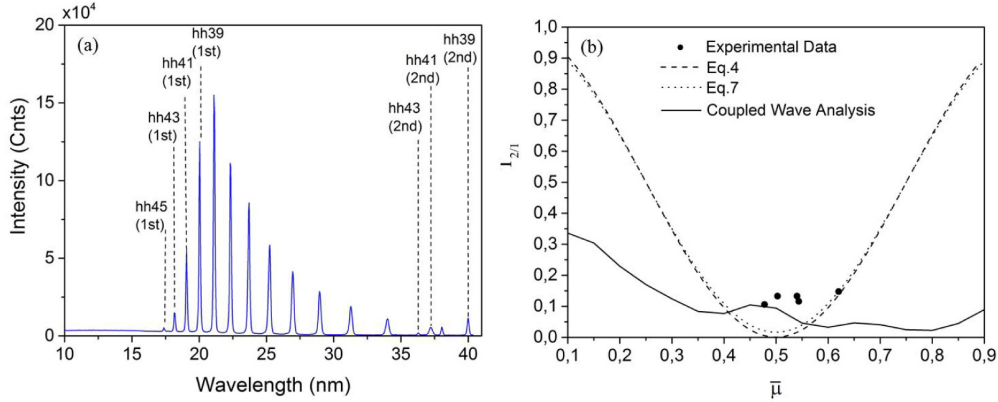


Fig. 7. (a) The high harmonic spectrum measured with a 10,000 lines mm^{-1} grating (G3). (b) Ratio of the second to first order diffraction efficiency measured at the 39th harmonic order ($\lambda = 20 \text{ nm}$) for five different gratings (black circles), second to first order diffraction efficiency calculated for a one-dimensional grating structure using Eq. (4) (dashed line) and Eq. (7) (dotted line), and for a two-dimensional grating, i.e. taking into account the finite thickness and also layered structure of the grating lines, based on a rigorous coupled wave analysis (solid line).

The spectra recorded with the five gratings show rather similar characteristics except for the relative height of the second-order diffraction peaks. The latter is quantified in Fig. 7(b), where the experimental values of $T_{2/1}$ for the gratings (G1-G5) with different $\bar{\mu}$ ratio are plotted as black circles. The values $T_{2/1}$ are obtained by taking the ratio of the spectrally integrated counts of the first and second diffraction orders for the 39th harmonic order (20.25 nm). This order is selected because it provides the highest signal in the 1st and 2nd diffraction order compared to the other harmonic orders. We now compare, as a first step, the experimental values of $T_{2/1}$ with the simple Fraunhofer theory for a one-dimensional grating as given in Sect. 2.1. For this case we take Eq. (4) with $m = 2$, which is plotted in Fig. 7(b) as the dashed curve. It can be seen that one of the experimental data points matches well with theory but that the other data deviate noticeably. To investigate whether fabrication imperfection is the cause for deviation, we have recalculated the ratio $T_{2/1}$, however, by taking into account the distribution of $\bar{\mu}$ -values that are found in the fabricated gratings. For a quantification we have used a Gaussian distribution as weighting factor for Eq. (4). The fabrication error averaged efficiency ratio is then given by

$$T_{2/1}(\bar{\mu}) = \int_0^1 \left(\frac{1}{\sigma\sqrt{2\pi}} e^{-\frac{(\mu-\bar{\mu})^2}{2\sigma^2}} \right) \left(\frac{\sin(2\pi\mu)}{2\sin(\pi\mu)} \right)^2 d\mu, \quad (7)$$

where the first bracket in the integral represents the Gaussian distribution function and the second bracket is taken from Eq. (4) for $m = 2$. The dotted curve in Fig. 7(b) shows a calculation of $T_{2/1}$ vs. $\bar{\mu}$ using Eq. (7) with $\sigma = 0.04$ which is the standard deviation obtained from the SEM images averaged over the five available gratings. We observe that the dotted curve yields a slightly higher $T_{2/1}$ ratio as compared to the dashed curve, yet, having taken into

account the experimental fabrication error via an averaging does not well explain the experimental $T_{2/1}$ values. We believe that the poor match of both the curves obtained with Eqs. (4) and (7) is due to the approximation of the gratings being one-dimensional, i.e. having a thickness of zero in the longitudinal direction. To take the finite thickness of the gratings into account, i.e. that the grating lines have a finite thickness and consist of three different material layers (Si_3N_4 200 nm, Au 70 nm, and Cr 12 nm), we have applied a Rigorous Coupled Wave Analysis (RCWA) method [19] to calculate the grating diffraction efficiencies. The RCWA is a semi-analytical method which determines the 1st and 2nd order diffraction efficiencies by solving Maxwell's equation in Fourier space for the incident beam which propagates through each grating line material. The calculated efficiency, $T_{2/1}$, is plotted as a function of $\bar{\mu}$ as the solid curve in Fig. 7(b). It can be seen that this solid curve shows a much better agreement with the measurement values than was obtained with Eqs. (4) and (7). We note, although $T_{2/1}$ is weakly wavelength dependent, that there is no significant change (less than 0.5%) within the finite spectral bandwidth of the considered harmonic. We assume that the remaining discrepancies are due to an unknown tilt-angle of the incident beam [20, 21] or due to a slightly trapezoidal profile [22] that may have been caused in fabrication. The analysis and control of the actual grating cross sectional geometry as well as the tilt angle would require further investigation which is beyond the scope of this paper. Nevertheless, the shape of the RCWA theoretical curve reveals that the $T_{2/1}$ does not vary very strongly as the $\bar{\mu}$ ratio deviates from the ideal value of 0.5. An according experimental verification might therefore require the fabrication of gratings with a wider range of $\bar{\mu}$ ratios. We note that the measured $T_{2/1}$ ratios for our gratings are considerably lower than what have been achieved with other high-density transmission gratings based on a different fabrication method [23]. Thus, the UV-NIL method used in the fabrication of our gratings appears to deliver a greater accuracy in the space-to-period ratio compared to other methods.

The measured spectra enable another important investigation, which is the comparison of the experimental spectral resolution provided by the grating spectrometer, $\Delta\lambda_{\text{ex}}$, with the theoretically expected resolution, $\Delta\lambda_{\text{th}}$, according to Eq. (6). The evaluation of the equation requires some assumption on the diameter, ΔS , of the high harmonic source area because a direct measurement is difficult. We estimate a source diameter of $\Delta S = 35 \mu\text{m}$, using a divergence measurement (beam diameter of 7 mm at a distance of $R_s = 9 \text{ m}$) and assuming that the high harmonic radiation propagates as a Gaussian beam. We note that this assumption describes diffraction limited beam propagation and therefore yields a lower limit for the source diameter. Using $\Delta S = 35 \mu\text{m}$ and inserting the source and detector distances and the size of the aperture used in our setup ($R_s = 9 \text{ m}$, $R = 120 \text{ mm}$, and $A = 100 \mu\text{m}$, $p = 26 \mu\text{m}$, respectively) we obtain $\Delta\lambda_{\text{th}} = 0.09 \text{ nm}$ for the range between 17.5 and 40.5 nm wavelength.

Retrieving the experimental spectral resolution, λ_{ex} , from the high harmonic spectrum in Fig. 7(a) requires deconvolving from the spectral width, w_q , of a single maximum in Fig. 7(a) the spectral bandwidth of the corresponding harmonic radiation, $\Delta\lambda_q$. The strongest peak in Fig. 7(a), which belongs to the 37th harmonic near $\lambda = 21 \text{ nm}$, shows a FWHM of $w_{37} = 0.13 \text{ nm}$ based on a Gaussian fit. For determining the smallest possible spectral bandwidth of the 37th harmonic we apply a Fourier argument. The maximum possible duration of emission at a high harmonic frequency is that of the drive laser pulse, however, the real limit lies at some shorter duration, for instance a factor of 0.7 shorter was observed in [24]. Using the drive laser and focusing parameters given above, with the peak intensity of $2.6 \times 10^{14} \text{ W/cm}^2$ and assuming a Gaussian temporal profile for the pulse duration of 39 fs (FWHM), we estimate the duration of the 37th harmonic with the following considerations.

The duration corresponds to the time interval of the drive laser pulse from the earliest moment of emission until phase matching is lost due to a critical level of ionization. The emission starts when the drive laser reaches the cutoff intensity [18] calculated to be $2.0 \times$

10^{14} W/cm², which is reached at 11 fs before the peak intensity. It shows that the generation process is not terminated by ionization because the critical ionization fraction [25] of 0.19% for Ne gas is not reached in our case (our ADK model calculations [26] yield an ionization of only about 0.05%). From this we conclude that the emission of the 37th harmonic terminates only when the drive intensity drops below the cutoff intensity again, which is at 11 fs after peak intensity. This yields an estimated pulse duration of the harmonic, $\tau_{37} = 22$ fs. Assuming a Gaussian pulse shape, we obtain a Fourier limited spectral bandwidth of the 37th harmonic of $\Delta\lambda_q = 0.03$ nm. This is a lower-limit value because any chirp or shorter duration of the harmonic would yield bigger values.

The deconvolution, assuming Gaussian line shapes then yields an upper value for the experimental resolution of $\lambda_{ex} < 0.13$ nm. This value compares well with theoretically predicted value of 0.09 nm, when taking into account the remaining uncertainty in the source diameter and HH radiation bandwidth as named above.

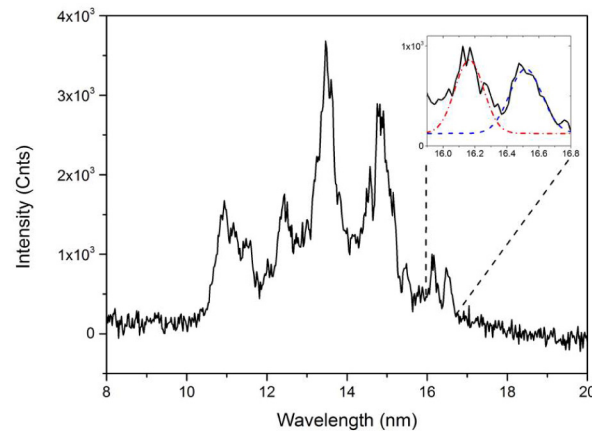


Fig. 8. Xenon discharge plasma spectrum measured with a 10,000 lines mm⁻¹ grating. The inset in Fig. 8 indicates the decomposition of the peaks corresponding to the 4d-5p transition features for Xenon.

To characterize the spectral resolution of our grating spectrometer also in combination with EUV sources of direct relevance for EUV lithography we used a second source which is based on a Xenon plasma generated by a discharge [27]. The setup is analogous to Fig. 1(a), with $\Delta S = 570 \mu\text{m}$, $A = 25 \mu\text{m}$, $p = 13.5 \mu\text{m}$, $R = 60$ mm and $R_s = 1.5$ m. Figure 8 shows a spectrum of the plasma source measured with our spectrometer over a range from 10 nm to 17 nm. Compared to the high harmonic source, the spectrum exhibits a higher complexity with partly overlapping lines, but the advantage is the much stronger average output power at 13.5 nm. The spectral features that we selected for an evaluation are the two peaks at 16.15 nm and 16.5 nm (Xe IX 4d-5p transitions [27]) because these two peaks are almost non-overlapping. Using a decomposition into two Gaussian peaks [see inset in Fig. 8], we obtain a FWHM of about $w_{Xe1} = 0.21$ nm for the first peak at 16.15 nm and $w_{Xe2} = 0.24$ nm for the second peak at 16.5 nm. To obtain the experimental spectral resolution, λ_{ex} , we select the narrower peak, w_{Xe1} for deconvolution with the spectral bandwidth of the corresponding Xenon radiation, $\Delta\lambda_{Xe1}$. The latter value was obtained from [27] as $\Delta\lambda_{Xe1} \geq 0.13$ nm. The deconvolution gives an upper value for the experimental resolution of $\lambda_{ex} < 0.17$ nm. For comparison we insert into Eq. (6) the experimental parameters and obtain $\Delta\lambda_{th} = 0.11$ nm which is well consistent with the experimental resolution.

In summary of the resolution measurements, using as an XUV source both HHG and a Xe discharge plasma, we find a spectral resolution that is close to the theoretically possible value. From this we conclude that the UV-NIL based fabrication method demonstrated here indeed

provides high-density XUV gratings with superior quality. Furthermore, the XUV source based on HHG has shown to be an excellent source for optical characterization of such gratings for its unique features, namely, the well-separated odd harmonics and the narrow-bandwidth of the individual harmonic order.

4. Conclusion

We have fabricated high-line-density transmission gratings for the XUV range using a nano-imprint lithography (NIL) method. The fabrication process is robust and reproducibly delivers high line-density gratings. SEM inspection shows space-to-period ratios in the range of 0.48 to 0.62 close to the intended ratio of 0.5 and a high degree of reproducibility, in the order of 4 nm for the width of gratings lines. The quality of the transmission grating was optically characterized by measuring emission spectra from a HHG-based and a plasma-based EUV source. The results show that the measured ratios of the second to first order diffraction efficiency, $T_{2/1}$, are as low as desired, in the range of 0.1 to 0.15, as compared to the almost four-times higher values around 0.37 that were reported for other gratings [23]. The optical characterization using the HHG source has shown a grating resolution with an upper-limit of 0.13 nm which matches the theoretically expected value of 0.09 nm. In summary, the fabrication method applied here proves to be very suitable for providing high quality, high-density transmission gratings for applications in the XUV range.

Acknowledgments

The grating development is enabled by funds from the FOM Valorization Prize, awarded in 2011 to Fred Bijkerk for his collective work on multilayer EUV optics. The authors also acknowledge the Industrial Partnership Programme ‘Controlling photon and plasma induced processes at EUV optical surfaces (CP3E)’ of the ‘Stichting voor Fundamenteel Onderzoek der Materie (FOM)’, which is financially supported by the ‘Nederlandse Organisatie voor Wetenschappelijk Onderzoek (NWO)’, and co-financed by Carl Zeiss SMT and ASML. This research program is also funded by the Technology Foundation (STW) under contract 10759. The latter research program is additionally supported by FERMI@Elettra and Coherent Europe BV.